Nanoscale

Accepted Manuscript

This article can be cited before page numbers have been issued, to do this please use: A. L.Y. Brabant, P. Knight, K. Joyce, M. Elabbadi, V. Lomonosov, C. Boukouvala and E. Ringe, *Nanoscale*, 2026, DOI: 10.1039/D6NR00806B.

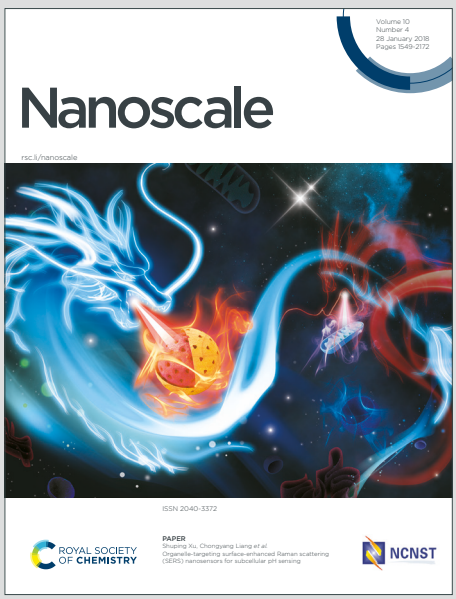

ROYAL SOCIETY OF CHEMISTRY

rsc.li/nanoscale

View Article Online
DOI: 10.1039/D6NR00806B

The reactivity of single magnesium nanoparticles towards corrosion and galvanic replacement†

Ambre L.Y. Brabant,[a] Pip J. Knight,[b] Kitty Joyce,[b] Mohsen Elabbadi,[b] Vladimir Lomonosov,[b] Christina Boukouvala,[b] Emilie Ringe[a,b]*

a. Department of Earth Sciences, University of Cambridge, Downing Street, Cambridge CB2 3EQ, United Kingdom
b. Department of Materials Science and Metallurgy, University of Cambridge, 27 Charles Babbage Road, Cambridge CB3 0FS, United Kingdom

† Electronic supplementary information (ESI) available. See DOI:

Abstract

Magnesium (Mg) nanoparticles are promising for plasmonic applications due to their wide resonance range, biocompatibility, and low cost. The low reduction potential of Mg leads to high reactivity, a double-edged sword yielding fast corrosion in water but also opportunities for synthetic strategies based on galvanic replacement. This study uses single particle dark field scattering to monitor the real-time dynamics of Mg nanoparticle corrosion and galvanic replacement by Pd, Cu, Pt, and Au. We find that while corrosion is immediate and gradual, galvanic replacement typically exhibits a significant induction stage, lasting up to two hours, followed by a rapid reaction phase. Results indicate that the induction stage is likely governed by the hydration and breakdown of the protective, native MgO surface. Consistent with this explanation, the duration of the induction stage decreases with increasing precursor concentration, decreasing pH of the metal precursor, and with the addition of water or NaCl known to accelerate MgO hydration. These mechanistic insights provide a foundation for designing the synthesis of Mg-based bimetallic nanostructures for plasmonic applications, as demonstrated for the Mg-Cu system in this paper.

View Article Online
DOI: 10.1039/D6NR00806B

Introduction

Localised surface plasmon resonances (LSPRs) are light-driven coherent oscillations of conduction electrons in metallic nanoparticles (NPs) that lead to strong, wavelength-dependent optical absorption, scattering, and enhancement of the local electric field. The understanding and control of LSPRs has flourished over the past decades, paving the way for multiple established and potential applications of plasmonic structures, ranging from biosensing to light-enhanced reactions and cancer ablation. A challenge in the engineering of plasmonic-powered effects is the limited number of materials capable of sustaining LSPRs at visible and near-infrared wavelengths, useful for solar harvesting and in-vivo applications, respectively.

Mg is a plasmonic metal attracting growing interest.[1–8] Indeed, Mg NPs can sustain LSPRs across the ultraviolet, visible, and near-infrared range, with a plasmonic quality factor better than Al's in the 300–900 nm range, and better than Cu and Au at wavelengths below 500 nm.[9] Mg is also earth-abundant (8th most abundant element in the crust) and biocompatible (Mg^{2+} is an essential nutrient). However, persistent concerns about Mg NPs include their safety and reactivity. The reactivity of Mg is rooted in its low reduction potential of −2.37 V vs standard hydrogen electrode.[10] Mg reacts with O_2, even at very low partial pressures, to form MgO, a stable, self-limiting surface oxide.[11] While the stability of plasmonic Mg NPs protected with native MgO in air has been demonstrated up to 400°C and in moist air between 200-400°C,[10] their reaction in water is rapid and leads to "transient", i.e., erasable, structures.[7]

Mg's reactivity and thermodynamically stable species in water are potential and pH-dependent, as described in its Pourbaix diagram.[12] Without an applied potential, Mg corrodes to Mg^{2+} ions below pH 11. The low reduction potential comes with advantages, too, as galvanic replacement of Mg is thermodynamically favourable for most d-block metals, and this reaction has been used as a synthetic strategy to produce decorated structures,[13–17] including Mg-Pd and Mg-Au architectures used in plasmon-enhanced catalysis.[16–18]

View Article Online
DOI: 10.1039/D6NR00806B

While the outcome, at the bulk level, of surface oxidation, corrosion, and galvanic replacement of Mg NPs is increasingly well understood, recent advances in nanoscience indicate that bulk observations and single particle reactivity can be strikingly different, the latter offering real reaction mechanism insights. For instance, Smith et al. demonstrated that galvanic replacement of Ag by Au is much faster at the single particle level than when viewed as an ensemble and exposed the importance of pit formation in the replacement process.[19] Further, Sterl et al. showed the importance of individual crystals in the dynamics of hydrogen absorption in polycrystalline Mg disks.[20]

Here, we interrogate the time-resolved, single particle level behaviour of Mg corrosion and galvanic replacement by a variety of metals. The changes in optical scattering from plasmonic Mg NPs is first numerically modelled to understand the expected size dependence. Then, the time-resolved scattering response of a large number of single particles is used as a proxy for reaction progress, leading to the observation of reaction rates correlating with water concentration. Next, this approach is applied to galvanic replacement of Mg with Pd, Cu, Au, and Pt, highlighting not only rapid reactions at the single particle level, but also the effect of corrosion-enhancing co-agents including water and NaCl. Lastly, we implement the insights from single particle studies to design an experiment for the bulk galvanic replacement of Mg by Cu. Together, these results reveal the dynamics of corrosion and galvanic replacement of plasmonic Mg NPs, providing a framework to design synthetic strategies for bimetallic structures.

Materials and methods

Nanoparticle synthesis

Platelet Mg NPs, hexagonal in shape, were synthesised by a procedure described in Wayman et al.,[21] i.e., by the reduction of $MgBu_2$ by lithium naphthalenide in THF in the presence of poly(vinylpyrrolidone) M_w = 10,000. Faceted spheroidal Mg NPs were synthesised by a seed-mediated reduction procedure described in Lomonosov et al.[22] Size distributions obtained from

View Article Online
DOI: 10.1039/D6NR00806B

secondary electron microscopy (SEM) images are reported in Figure S1. The average length (longest axis as measured in images) of the faceted spheroidal NPs was 132 nm (standard deviation 20 nm), with an average aspect ratio of 1.2, while the average length of the platelet Mg NPs (longest axis) was 520 nm (standard deviation 232 nm), with an average aspect ratio of 2.0.

Dark field optical microscopy

Reactions of Mg NPs with water and metal salts were studied in-situ in a darkfield optical setup (Figure 1) in a Nikon Eclipse Ti2 inverted optical microscope as described in Kumar et al.[23] White light from a Nikon D-LH/LC 12V 100W halogen lamp was directed through a Nikon dark field condenser with numerical aperture (NA) 0.80-0.95. A Nikon CFI Plan Fluor 100XS oil immersion objective lens with NA set to 0.5 collected the light scattered by the sample, which was directed either to a Thorlabs CS505CU Kiralux 5.0 MP Color CMOS Camera or a Princeton Instruments IsoPlane SCT320 spectrometer fitted with a 50 g/mm grating followed by a Princeton Instruments ProEM HS 1024 × 1024 EMCCD (Na_2PdCl_4, $HAuCl_4$, and Na_2PtCl_4 reactions) or a Princeton Instruments PIXIS 256E CCD (H_2O and $CuCl_2$ reactions).

In each experiment, a glass cover slip was rinsed with isopropanol before drop-casting 4-10 µL of a 0.3-0.6 mM suspension of NPs in isopropanol. The Mg NPs were then put into contact with a liquid reagent inside the microscope using one of three setups shown in Figure S2. In the drop setup, 50 µL of reagent was pipetted onto the slide. In the open-cell setup, a piece of 2.5 mm thick silicone with a 1 cm x 1 cm square hole was placed on the cover slip and 250 µL of reagent was pipetted into the hole. In the closed-cell setup, the top surface of the cell was sealed with a second glass cover slip. The drop setup was used for reactions taking seconds to minutes and the closed-cell setup for those lasting > 10 minutes to minimize the impact of solvent evaporation. The open-cell setup was used for reactions in ethanol, taking seconds to minutes, for which a drop setup was not appropriate due to rapid evaporation in the illuminated regions.

Single particle reactions

View Article Online
DOI: 10.1039/D6NR00806B

Water: Faceted spheroidal Mg NPs were exposed to mixtures of isopropanol and deionised water with water concentration varying from 10 vol.% to 60 vol.%. Experiments were carried out in the drop setup (except 10 vol.%, closed-cell setup) and recorded with the colour camera at a rate of 0.2-1 frames per second (fps).

Palladium: Platelet Mg NPs were exposed to solutions of Na_2PdCl_4 (99.99%, Sigma-Aldrich) in isopropanol ranging from 0.5 mM to 2.0 mM. Experiments were also carried out with 0.5 mM Na_2PdCl_4 + 2 mM NaCl (99.95%, Fisher Chemical), and with 1.5 mM Na_2PdCl_4 + 1 vol.% water. Experiments were carried out in the closed-cell setup and recorded with the colour camera at 0.025-0.1 fps. Additional reactions with 1.0 mM Na_2PdCl_4, reported in the ESI, were recorded with the spectrometer every 4 min.

Copper: Faceted spheroidal Mg NPs were exposed to $CuCl_2$ (99%, Sigma-Aldrich) in ethanol at concentrations between 0.1 mM and 7.4 mM; ethanol was chosen as the solvent for $CuCl_2$ to allow for a large concentration range. All experiments were carried out using the open-cell setup and recorded with the colour camera at 0.2-1.0 fps. Additionally, a reaction with 0.1 mM $CuCl_2$ was recorded in spectroscopy mode every 2.3 s.

Gold: Platelet Mg NPs were exposed to 0.05 mM $HAuCl_4$ (99.999%, Sigma-Aldrich) in isopropanol in the closed-cell setup and recorded with the colour camera at 0.5 fps.

Platinum: Platelet Mg NPs were exposed to 1.0 mM Na_2PtCl_4 (99.95%, Alfa Aesar) in isopropanol in the closed-cell setup and recorded with the colour camera at 0.5 fps.

In all reactions, reagents were in excess of Mg. Water was in excess by a factor of $>10^4$; metal salts were in excess by factors ranging from approximately 3 to 300.

In a given experiment, 16-44% of intensity-time series with Na_2PdCl_4 contained more than one step and 17-56% for $CuCl_2$ (Table S1); such series may correspond to small aggregates in which different particles react at different times. These time series were not analysed for kinetics and are available upon request from the authors.

View Article Online
DOI: 10.1039/D6NR00806B

Colloidal galvanic replacement reactions

Colloidal faceted spheroidal Mg NPs (~ 2 mM) were exposed to 1.7 mM $CuCl_2$ in anhydrous ethanol (and just anhydrous ethanol for control experiments). Deionised water was added in concentrations of 0, 1.7, 3.3, and 8.3 vol.%. corresponding to 0, 0.1, 0.2, and 0.5 mL in the total 6 mL reaction volume. Reactions were stirred at room temperature for 10 minutes after mixing. Following this, reactants were removed by two cycles of centrifugation and redispersion in anhydrous ethanol and one cycle of centrifugation and redispersion in anhydrous isopropanol. NPs were redispersed in isopropanol, transferred to a PMMA cuvette, and UV-Visible extinction profiles were obtained with a Thermo-Scientific Evolution 220 spectrophotometer.

Data processing – imaging

Raw data from the colour camera consisted of stacks of images taken at regular time intervals and was processed using ImageJ. Firstly, a SIFT registration algorithm[24] built into ImageJ was used to correct for image drift if needed. Thresholding and automatic particle detection were then applied to extract the scattering intensity-time series of individual particles, with the intensity being averaged over the same particle area through the time series to ensure consistency. Particle intensity-time series were processed in Python including background corrections and automatic spike detection and removal.

In addition to the above processing, in the experiments with $CuCl_2$ the particles which disappeared in the time gap between adding the reagent and starting the recording (~10-30 s) were counted by comparing the first frame of the camera recording with an image taken before adding the reagent. Linear models were fit by least-squares regression to single particle intensity-time series from the experiments with $CuCl_2$, in the interval between 80% and 20% of the initial intensity (Figure 6). However, in a subset of cases for 0.1 mM $CuCl_2$, a line was fit down to only 50% if the time series diverged from linearity by sloping off to shallower gradients. Within the same reaction, the number of

View Article Online
DOI: 10.1039/D6NR00806B

particles from which a reaction gradient was obtained can be lower than the number of NPs for which an induction stage duration was measured, owing to particles decaying before the recording started.

Data processing – spectral time series

Spectra were background subtracted and divided by the lamp output profile (Figure S3) as described in Kumar et al.[23] The location of a particle in the slit was identified and averaged over three pixels along the spatial dimension to reduce noise. This gave the particle scattering intensity as a function of wavelength and time.

Electron microscopy

NPs were imaged from drop-cast solutions on indium tin oxide (ITO)-coated coverslips using a Nova NanoSEM L50 field emission gun SEM operated at 15 kV. All SEM images shown in the main manuscript were acquired with an Everhart-Thornley secondary electron detector. Additionally, the instrument was equipped with a concentric-backscattered detector and an Oxford Instruments energy dispersive X-ray spectrometer (EDS); results from these detectors are reported in the SI. SEM was also used to characterise the size distributions of Mg NPs used in the reactions (Figure S1). HAADF-STEM images were acquired on a FEI Osiris operated at 200 kV, with NPs drop-cast on carbon-coated Cu grids.

Numerical simulations

Scattering cross-sections for the faceted spheroidal NPs were calculated numerically with DDSCAT, a Maxwell solver using the discrete dipole approximation,[25] with an inter-dipole distance of 0.7-3.0 nm depending on the NP size. A Wulff construction using Crystal Creator[26] with surface energies from Lautar et al.[27] (Table S2) was used to approximate the shape of the faceted spheroidal NPs. A cuboidal glass substrate of thickness 40 nm and side length 80 nm + the tip-to-tip width of the faceted spheroidal NPs (*d* in Figure 2) was added to account for the effect of the glass cover slip. The dielectric function of Mg was taken from Palik,[28] the ambient refractive index was set to 1.38 (isopropanol), and the refractive index of the glass, to 1.52. Light was incident at 31° to the substrate

View Article Online
DOI: 10.1039/D6NR00806B

and polarised in a vertical plane; this reproduced the inclination of the light cone output by the dark field condenser and was a good approximation for unpolarised light given the 1.2 aspect ratio of the faceted spheroidal NPs. Scattering cross-sections (σ) were calculated for wavelengths (λ) between 400 nm and 900 nm in 10 nm steps. The expected relative intensity in the colour camera was then calculated as follows:

$$I_d = \sum_{i=R,G,B} \int_{400nm}^{900nm} S_i(\lambda) \cdot \sigma(\lambda) \cdot \frac{L(\lambda)}{S_g(\lambda) \cdot S_d(\lambda)} d\lambda \quad (1)$$

Where I_d is the relative intensity measured by the camera, L is the lamp spectrum measured with the spectrometer (Figure S3), and S_d, S_g, S_i are the spectral responses of the CCD, spectrometer grating, and i^{th} channel of the colour camera respectively (spectral responses provided by Thorlabs and Princeton Instruments). The integrand was numerically integrated over wavelength and summed over the three channels of the colour camera.

A surface film consisting of MgO and/or $Mg(OH)_2$ is expected to be present on the NPs at all times; studies of the reaction of Mg with water show variability in the structure, thickness, and composition of this film, suggesting its sensitivity to experimental conditions.[29–39] Because of the uncertainty in the characteristics of the surface film, for simplicity the NPs were modelled without oxides, and considering the trends rather than aiming for a quantitative match. We do not expect this approximation to significantly affect the derived conclusions, because previous numerical results show that the presence of an MgO shell shifts LSPRs to longer wavelengths with little effect on the LSPR intensity.[40,41]

View Article Online
DOI: 10.1039/D6NR00806B

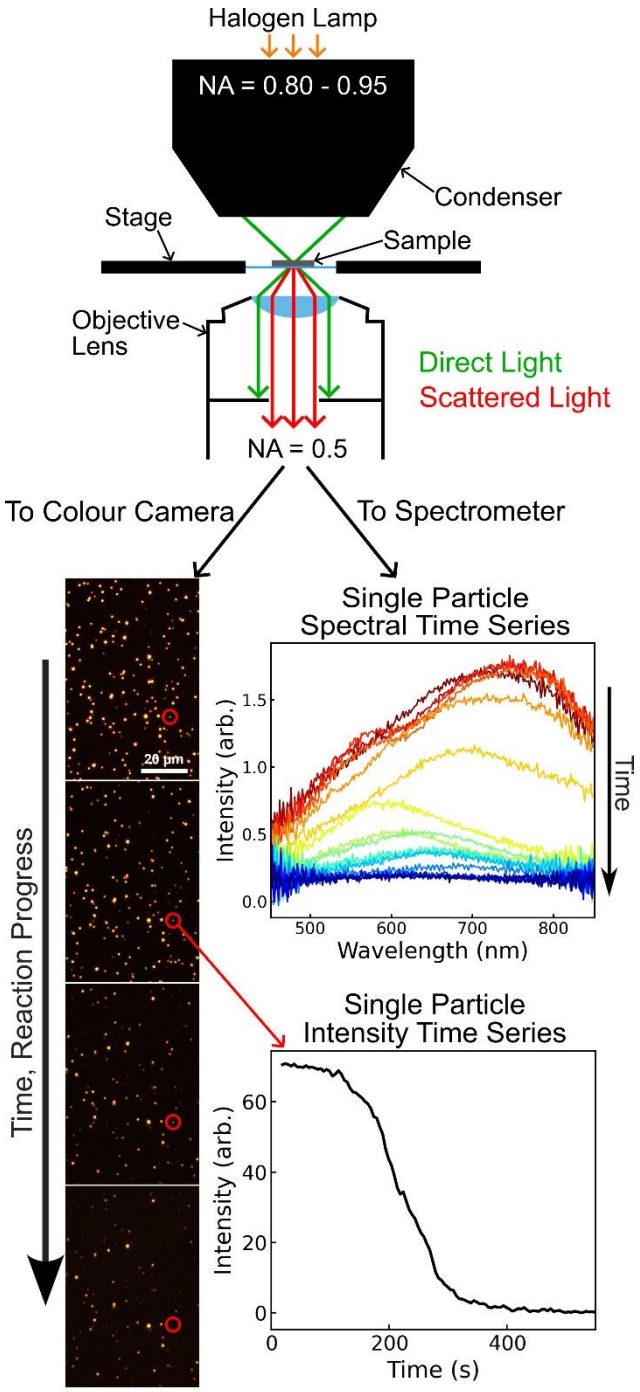

Figure 1. Single particle darkfield optical scattering. A hollow cone of white light is directed to a drop-cast Mg NP sample, leading to scattering collected in imaging (camera) or spectroscopy (spectrometer and CCD) mode. Time series of the total scattering intensity are extracted in imaging mode, while time series of the scattering spectrum are extracted in spectroscopy mode.

View Article Online
DOI: 10.1039/D6NR00806B

Results and discussion

Reactivity in water

We first explore numerically the changes in optical scattering of a Mg NP as its size decreases, mimicking a reaction with water. Smaller NPs are expected to produce a lower LSPR intensity and higher resonance energy.[42,43] Simulations of the dark field scattering spectrum of faceted spheroidal Mg NPs with various diameters *d* (Figure 2a), on a 1.52 refractive index (RI) glass substrate and immersed in an isopropanol medium (RI = 1.38) were obtained using the discrete dipole approximation.[25] Results confirm the expected intensity and wavelength shifts (Figure 2b), while the total intensity expected experimentally, corrected for the wavelength-dependent sensitivity of the optical setup, decreases monotonically with NP size (Figure 2c).

To probe corrosion experimentally, Mg NPs were synthesised using a previously reported colloidal reduction procedure, yielding faceted spheroidal NPs (Figure 3a,b) with an average side length of 132 nm (standard deviation 20 nm, Figure S1). Bulk corrosion experiments were first performed (Figure S4), showing the decrease in LSPR intensity of Mg NPs over time in 5 vol.% water in isopropanol. This ensemble-averaged data is difficult to interpret, however, because water-induced aggregation cannot be separated from the effects of the reaction itself, and neither can the signal from single NPs and that of aggregates. Therefore, we turned to single particle studies, implemented in a dark field optical scattering microscope (Figure 1) equipped with a spectrometer/CCD for spectral acquisition as well as a colour camera for rapid, large-scale scattering intensity monitoring.

Time series of the scattering intensity of single faceted spheroidal NPs during reaction with water-isopropanol mixtures were approximately linear (Figure 3c), as evidenced by high R-squared values (Figure S5). Apparent reaction completion was reached between 20 s and 800 s for water concentrations between 10 vol.% and 60 vol.%, with the distribution of reaction times narrowing and shifting to lower mean times as the water concentration increased (Figure 3d-i). This observation is not an artefact of variable starting NP size distributions, as the same samples were used; as expected there was nostatistically significant difference between the distribution of single particle scattering intensity (a

View Article Online
DOI: 10.1039/D6NR00806B

proxy for size) at the start of the experiments with different water concentrations (Figure S6), nor any trends for the scattering intensity across the different experiments.

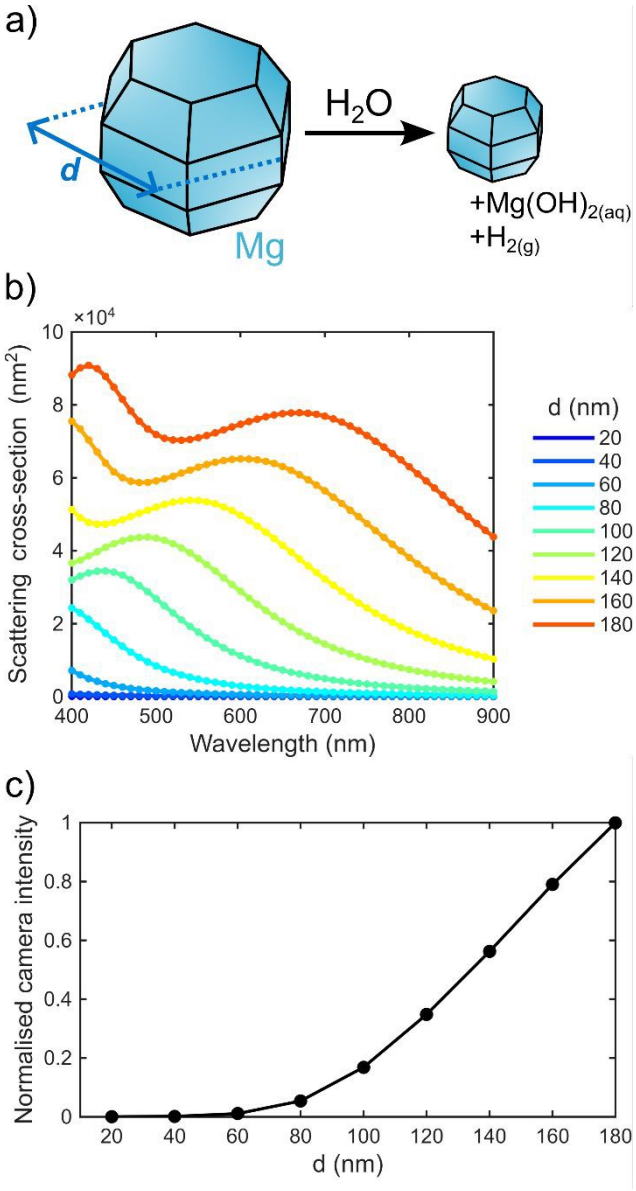

Figure 2. Numerical simulations of Mg NPs scattering. a) Schematic of the reaction of Mg NPs with water, showing the shape used to approximate the faceted spheroidal Mg NPs and the definition of the tip-to-tip distance *d*. b) Scattering cross-section as a function of *d*, for a Mg NP on a glass substrate in isopropanol. c) Calculated intensity in the colour camera as a function of *d*. Markers in b) and c) indicate calculated points.

View Article Online
DOI: 10.1039/D6NR00806B

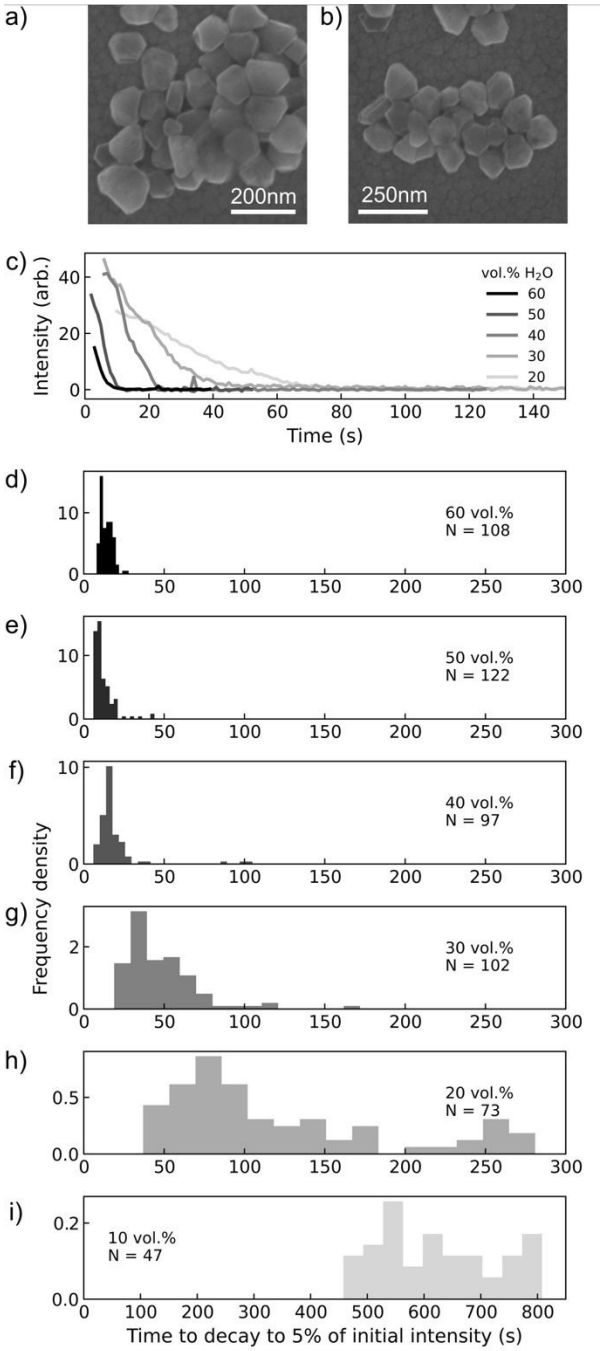

Figure 3. Corrosion of faceted spheroidal Mg NPs by water-isopropanol mixtures. a-b) SEM images of faceted spheroidal NPs before water exposure, for a concentrated suspension. c) Single particle scattering as a function of time for representative NPs from experiments at five different water concentrations. d-i) Distributions of decay time, defined as the time for the intensity to decay to 5% of its initial value, for different water concentrations. *N* is the number of particles in each distribution. Note that the time axis in i) is larger than in the other plots.

View Article Online
DOI: 10.1039/D6NR00806B

Tracking galvanic replacement reactions

Overview

Similarly to the tracking of Mg corrosion described above, single particle approaches also offer opportunities to explore the dynamics of galvanic replacement of Mg NPs by ions with more positive reduction potentials (most metals except the alkali).[44–46] Here, we further our exploration of single particle reactivity by investigating the galvanic replacement of Mg, shown schematically in Figure 4a. Briefly, Mg NPs were drop-cast and exposed to various concentrations of the metal ions in solution. We first investigate and compare the behaviour of the noble metals Pd, Au, and Pt using platelet Mg NPs. Then, we use spheroidal Mg NPs discussed above to delve in-depth in the understanding, then design, of galvanic replacement reactions by Cu.

SEM images (Figures 4b, S7-S9) and SEM-EDS spectra (Figure S7) of the structures produced by partial reactions (quenched after variable reaction times by rinsing with isopropanol) indicate that the contrast of the Mg core, a proxy for thickness, decreases as Mg is oxidised to Mg^{2+}, while the replacing metal (initially an oxidised salt in solution) is reduced and deposited as a solid on the surface of the Mg core. The morphology of the deposited metal, discrete islands rather than continuous layers, is consistent with previous results for bulk GR studies.[44] Note that there is no miscibility between the Mg and the replacing metals investigated here (Pd, Pt, Au, Cu),[48–51] so that alloying between the replaced and replacing metals is unlikely to play a role, unlike in the galvanic replacement of Ag by Au.[19]

The appearance of Pd islands in the galvanic replacement of platelet Mg NPs by Na_2PdCl_4 is time-dependent, with no Pd structures observed in the first 15 mins of the reactions with 0.5 mM and 1.0 mM Na_2PdCl_4. Pd appears earlier at higher concentrations, visible after 7.5 minutes at 1.5 mM (Figure S8). While instructive of the morphology of replaced structures, such quenched experiments provide little insight into the reaction kinetics.

View Article Online
DOI: 10.1039/D6NR00806B

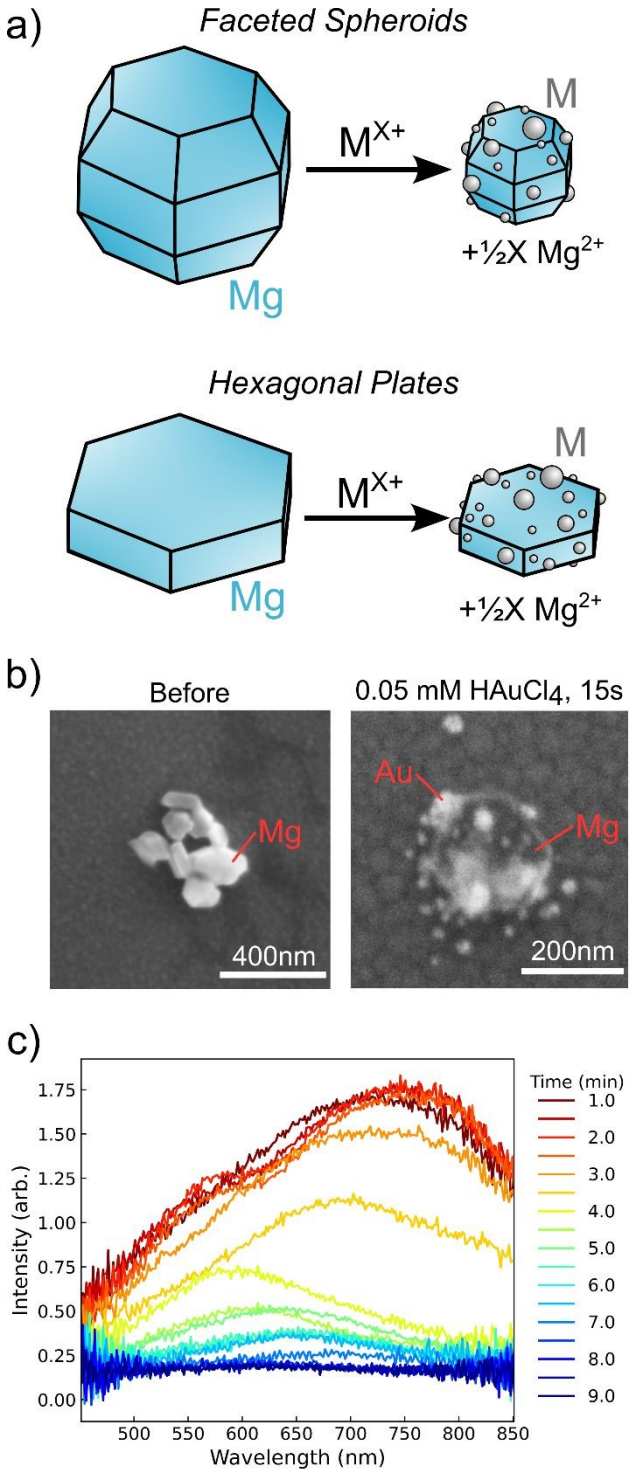

Figure 4. Galvanic replacement reactions. a) Schematic representation of the galvanic replacement reaction between a Mg NP and a metal salt. b) SEM images of Mg NPs to which no reagent has been added, and a Mg NP that has reacted with 0.05 mM $HAuCl_4$ for 15 seconds, displaying metallic Au decorations. c) Experimental scattering spectrum of a single faceted spheroidal Mg NP as a function of time during reaction with 0.1 mM $CuCl_2$.

View Article Online
DOI: 10.1039/D6NR00806B

By consuming the Mg core and depositing another metal, galvanic replacement is expected to affect the optical scattering of the NPs, providing means to track reaction progress in real time. Experimentally, the LSPR scattering intensities decreased as reactions proceeded, while resonance wavelengths shifted in variable directions (Figure 4c for Cu and Figure S10 for Cu and Pd). Upon reaction completion, the scattering signal essentially vanished (Figure 4c for Cu, Figure S10 for Cu and Pd, and Figure S11 for Au, Pt, and Pd), even when the replacing metal itself was plasmonic (e.g., Cu and Au). This is likely due to Cu oxidation and the production of Au nanostructures too small to significantly scatter.[42]

Since the addition of small metal decorations does not significantly contribute to the experimentally observed optical response, the modelled size dependence of the scattering of a faceted spheroidal Mg NP (Figure 2) still applies: the single particle intensity in the camera decreases monotonically with NP size; this also applies to platelet Mg NPs (Figure S12).

Galvanic replacement by Pd

The partial reaction of platelet Mg NPs with Na_2PdCl_4 produced Mg cores decorated by Pd NPs (Figures S7 and S8) as previously reported by Lomonosov et al.[16] The products of complete galvanic replacement displayed only Pd, sometimes loosely attached to small fragments of oxidized Mg (Figure S8).

Intensity-time series of single platelet Mg NPs reacting with Na_2PdCl_4 consisted of two distinct stages (Figure 5a). The induction stage, lasting up to two hours where little to no change in intensity was observed, preceded a sharp decrease to noise-level scattering intensity (the reaction stage) for Na_2PdCl_4 concentrations between 0.5 mM and 2.0 mM. This behaviour starkly contrasts with the gradual and linear decrease in scattering intensity during the corrosion reaction and is very similar to the Ag replacement by Au observed by Smith et al.[19] Spectrally resolved time series also confirm the

View Article Online
DOI: 10.1039/D6NR00806B

presence of induction, showing the overall scattering profile staying constant before undergoing a sharp overall intensity drop (Figure S10).

The distribution of induction stage durations shifted to shorter mean times and narrowed with increasing Na_2PdCl_4 concentration (Figure 5b,c,e,f), similarly to the replacement of Ag by Au.[19] The reaction was very fast compared to the sampling needed to measure the induction stage (in all experiments except at 0.5 mM Na_2PdCl_4, up to 82% of reactions completed within 20s) so that a rate could not reliably be extracted for the reaction stage.

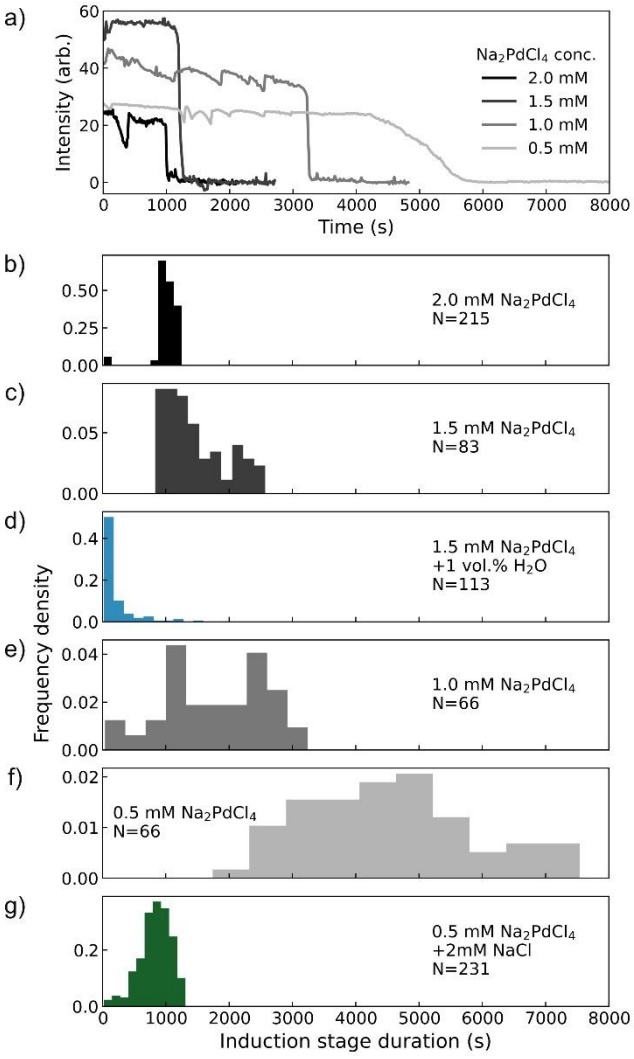

Figure 5. Galvanic replacement of platelet Mg NPs with Na_2PdCl_4. a) Single particle scattering intensity as a function of time for representative NPs from experiments at four different concentrations. Defocussing and refocussing in the microscope led to dip-like features observed

View Article Online
DOI: 10.1039/D6NR00806B

concurrently for all particles within an experiment. b-g) Distributions of induction stage duration, defined as the time for the intensity to decay to 60% of its initial value.

Smith et al.[19] attributed the induction stage to the time needed to form a void of a critically stable size in the Ag NP undergoing galvanic replacement. Here, the induction stage could similarly represent the time taken to form a critically stable nucleus of Pd metal on the surface of the Mg core, after which the reaction can proceed rapidly. Despite this explanation being consistent with the shortening of the induction stage with increased concentrations of Na_2PdCl_4, it cannot account for extremely long induction times (up to 2h). Indeed, due to the large difference in the reduction potentials of Mg and Pd, the characteristic time of Pd nucleus formation is expected to be moderately short.

To describe the oxidative action of hydrogen peroxide on Ag NPs, Naik et al.[45] described a "sawing" mechanism, where Ag NPs are broken up into multiple smaller NPs. This mechanism is unlikely here: the smooth nature of single particle intensity-time series decay suggests progressive dissolution of Mg NPs rather than multiple sawing events.

Alternative to these explanations, the prolonged induction behaviour can be attributed to mass transport limitations observed at the initial stages of galvanic replacement. Due to high surface reactivity, as-synthesised Mg NPs are always covered with a thin (5-20 nm) native self-limiting oxide layer, which protects the NPs from further oxidation.[11] The oxide layer is expected to substantially hinder galvanic replacement by acting as a mass-transport barrier, leading to the long induction times required for Pd ions to reach the Mg core. Consistent with this hypothesis, adding 1 vol.% water to the reagent mixture reduced the induction stage duration from 15-40 min to < 5 min in most cases (Figure 5c vs 5d), by converting MgO into less passivating $Mg(OH)_2$.[29,46] Control experiments with 1 vol.% water in isopropanol and no Na_2PdCl_4 (Figure S13) show only a 40% loss in scattering intensity over 30 minutes, demonstrating that this acceleration of the induction stage does not simply result from direct oxidation of the Mg by water. Furthermore, when 2 mM NaCl was present during galvanic replacement of Mg NPs with 0.5 mM Na_2PdCl_4, the induction stage duration decreased from 30-125

View Article Online
DOI: 10.1039/D6NR00806B

min to < 20 min (Figure 5f vs 5g). Given Cl^- ions can accelerate the hydration of MgO,[47] the observed shortening of the induction stage by the addition of NaCl or the increase in Na_2PdCl_4 concentration (also affecting Cl^- concentration) is consistent with the hydration hypothesis.

The hydration of the MgO film should also be a relevant process in the reaction with water-isopropanol mixtures, in which, however, no induction stage is observed. The high concentration of water probably meant the hydration of MgO was too fast to appreciably affect the scattering intensity-time series or to produce an induction stage.

There is no correlation between single particle initial intensity and induction stage duration (Figure S14). Given the expected relationship between NP size and scattering intensity, this observation suggests the induction stage duration is independent of the starting Mg NP size, consistent with a mechanism involving the hydration of the (size-independent) MgO layer.

Similarly to the reaction with Pd, the partial reaction of platelet Mg NPs with $HAuCl_4$ and Na_2PtCl_4 produced Mg cores decorated with Au or Pt islands, while the complete reaction produced NPs consisting only of the replacing metal (Figures S9, S15), as confirmed by elemental analysis with SEM-EDS (Figure S7). The replacement of Mg by Pt displayed an induction stage of 100-150 s for 1.0 mM Na_2PtCl_4, with a narrow distribution of decay times (Figure S15). Meanwhile, for the replacement of Mg by Au, the induction stage, if present, was shorter than the experimental starting time (t*) of 30 s, and the reaction time was fast (50-250 s) considering the comparatively very low 0.05 mM $HAuCl_4$ concentration (Figure S15). The timescale of galvanic replacement for these metal salts thus goes, from slowest to fastest, as $Na_2PdCl_4 > Na_2PtCl_4 >> HAuCl_4$. The marked difference for the reactivity of Au is likely due to the formation of an acidic solution known to facilitate MgO hydration.[48]

Galvanic replacement by Cu

The galvanic replacement of Mg by Cu was performed for spheroidal Mg NPs; their narrow size distribution and shape homogeneity[22] allows the mitigation of potential size and shape effects on

View Article Online
DOI: 10.1039/D6NR00806B

single particle measurements. Similarly to the replacement of Mg by Pd, Pt, and Au, the partial reaction of Mg NPs with $CuCl_2$ produced Mg cores decorated by a Cu-dominated solid as evidenced by SEM-EDS (Figure S7). These decorations are likely an oxidised form of Cu resulting from water and air exposure during and/or after reaction. However, the absence of Cl in the EDS spectrum rules out precipitation of $CuCl_2$.

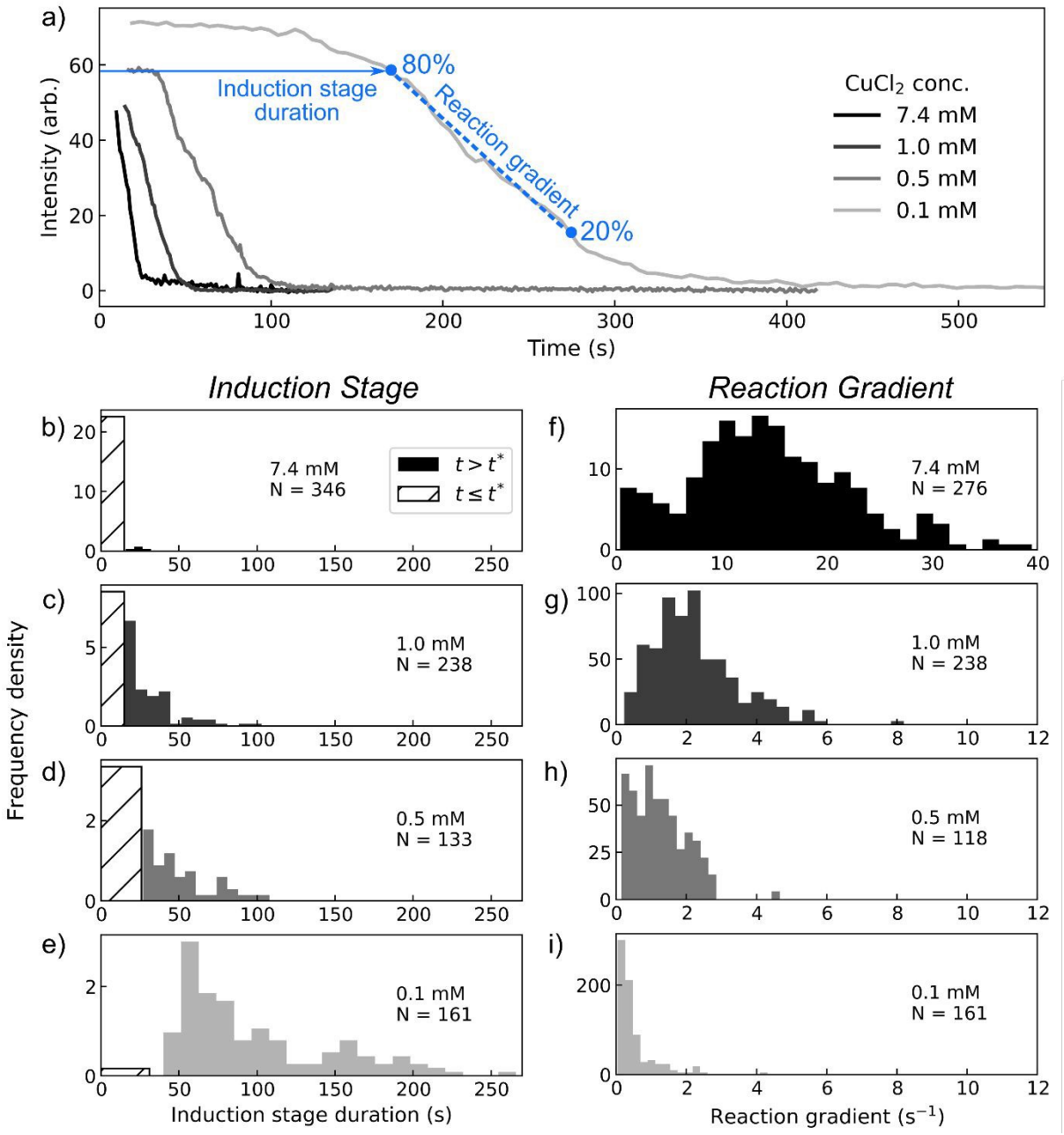

Figure 6. Galvanic replacement of faceted spheroidal Mg NPs with $CuCl_2$. a) Scattering intensity as a function of time for representative NPs from experiments at four different concentrations of $CuCl_2$.

View Article Online
DOI: 10.1039/D6NR00806B

Blue annotations define induction stage duration (time for the intensity to decay to 80% of its initial value) and reaction gradient (best-fit linear gradient between 80% and 20% of the initial intensity, barring exceptions set out in the methods). b-e) Distributions of induction stage duration for different concentrations of $CuCl_2$. When the induction phase duration t was less than the time t* between adding the reagent and starting the recording, the data is recorded as $t \leq t^*$. f-i) Distributions of reaction gradient for different concentrations of $CuCl_2$. The horizontal scale in f) is larger than in g-i).

The intensity-time series of single faceted spheroidal Mg NPs reacting with $CuCl_2$ (0.1-7.4 mM) also displayed an induction stage (up to ~260 s) followed by a decrease in scattering signal indicative of galvanic replacement (Figure 6a). The induction-reaction behaviour was also apparent in spectrally resolved intensity time series (Figures 4c, S10). Unlike the reaction with Na_2PdCl_4, the induction and reaction timescales were of the same order of magnitude, allowing the reaction stage to be resolved and analysed. Linear models were fitted to the reaction interval to use the intensity-time gradients as a proxy for the reaction rate; R-squared values > 0.9 (Figure S5) indicate that linear fits were suitable.

Increasing the concentration of $CuCl_2$ shortened the induction stage duration (Figure 6b-e). In some intensity time traces, no induction stage was observed after the start of the recording at ~30 s ($t \leq t^*$ in Figure 6); their proportion increased with $CuCl_2$ concentration (Figure 6b-e), suggesting again shorter induction stages for larger concentrations. Distributions of initial scattering intensities (a proxy for initial NP size) do not vary systematically with $CuCl_2$ concentration (Figure S6), and initial intensities and induction stage durations are not correlated (Figure S16).

Meanwhile, the reaction gradient increased with $CuCl_2$ concentration, indicating that the rate of the galvanic replacement correlated with Cu^{2+} concentrations.[55] The induction stage durations for $CuCl_2$ are shorter than those of Na_2PdCl_4 and Na_2PtCl_4, but longer than that of $HAuCl_4$. This is consistent with the pH trend of the salts, however the different shape used for Cu reactions (spheroids) and Pd, Pt, and Au (platelets) cannot be ruled out at this point to play a role in the reaction kinetics.

View Article Online
DOI: 10.1039/D6NR00806B

Designing galvanic replacement reactions

The mechanistic insights provided by single particle investigations can inform the design of bulk colloidal reactions. We conducted partial galvanic replacement reactions of colloidal faceted spheroidal Mg NPs with $CuCl_2$ in ethanol (with a 2:1.7 Mg:Cu ratio) in the presence of up to 8.3 vol.% water. Whereas no spectral changes occurred for particles kept in anhydrous ethanol or exposed to $CuCl_2$ in anhydrous ethanol after 10 minutes, the addition of water enabled galvanic replacement, as supported by the absorbance decay indicative of Mg oxidation (Figure 7). Control experiments with no $CuCl_2$ and the same water concentrations show no appreciable change in UV-Visible absorbance spectra over the same reaction time (Figure S17), ruling out a direct reaction with water. Further, clear evidence of Cu clusters on Mg for reactions with $CuCl_2$ in the presence of water contrasts with the smooth, uniform, and Cu-free NPs observed in anhydrous reactions (high-angle annular dark field STEM (HAADF-STEM) in Figure 7, additional HAADF-STEM and SEM in Figure S18), again indicating the enabling role of water in galvanic replacement of Mg by Cu. These results, using single particle insights, pave the way for further bulk reaction design utilising water as an initiator.

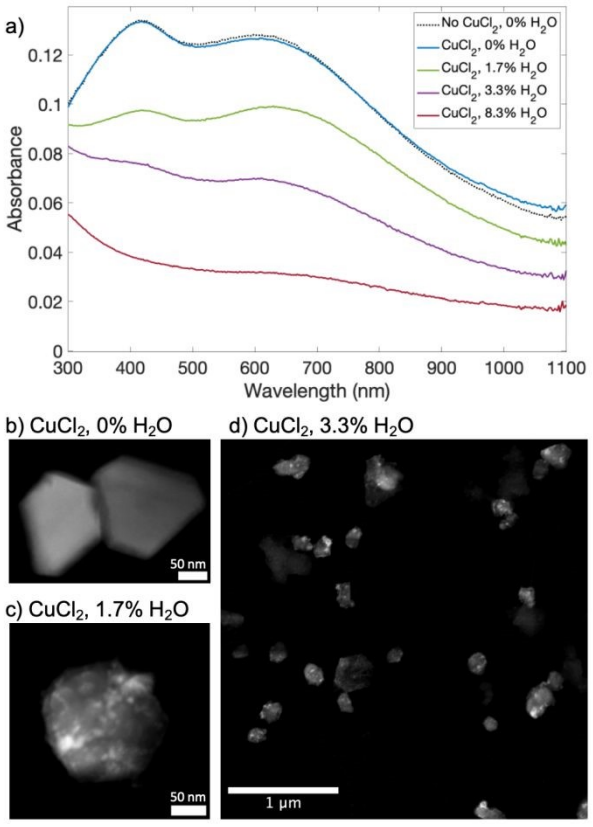

View Article Online
DOI: 10.1039/D6NR00806B

Figure 7. Water-assisted galvanic replacement. a) UV-Visible absorbance spectra of faceted spheroidal Mg NPs redispersed in isopropanol after 10 minutes of reaction with (and without) $CuCl_2$ and various concentrations of water. b-d) HAADF-STEM images of NPs after reaction, where Cu islands can only be seen in reactions involving water. Additional images reported in Figure S18.

Conclusions

The evolution of the scattering response of single Mg NPs during reaction with water (corrosion) and galvanic replacement by Pd, Cu, Pt, and Au was investigated. By systematically varying the concentrations of reactive species, observing reaction dynamics at the single particle level on a statistically relevant number of particles, and performing validating numerical calculations, we unravelled reaction processes otherwise invisible by bulk, ensemble-averaged approaches. Namely, corrosion starts immediately and occurs gradually, at a rate dependent on the water concentration. Meanwhile, in galvanic replacement by Pd, Cu, and Pt, we observed an induction stage before the start of the reaction. This induction stage lasted up to two hours and depended on the metal ion concentration and acidity. Significant shortening of the induction stage was observed when adding water or NaCl, pointing to the need for hydration and breakdown of the initially protective MgO layer for the reaction to proceed.

The knowledge gained from single particle studies, in particular the effect of water on the galvanic replacement of Mg NPs, was utilised to design the bulk reaction of Mg NPs with $CuCl_2$. Water addition enabled the creation of bimetallic structures without significantly affecting the optical properties bestowed by the underlying Mg.

Together, these mechanistic insights into the breakdown of the MgO layer and the galvanic replacement of Mg provide tools to design synthetic strategies for bimetallic nanostructures, where the core Mg can be retained for, e.g., its plasmonic properties and the decorating metals can be controlled in size and morphology to dictate their function, for instance as sensors or catalytic surfaces.

View Article Online
DOI: 10.1039/D6NR00806B

Author Contributions

A.L.Y Brabant: Data curation, Formal analysis, Investigation, Methodology, Validation, Visualisation, Writing – original draft, Writing – review & editing

P. J. Knight: Conceptualisation, Formal analysis, Investigation, Methodology, Validation, Visualisation, Writing – review & editing

K. Joyce: Conceptualisation, Formal analysis, Investigation, Methodology, Validation, Visualisation, Writing – review & editing

M. Elabbadi: Conceptualisation, Formal analysis, Investigation, Methodology, Visualisation, Writing – review & editing

C. Boukouvala: Formal analysis, Validation, Investigation, Methodology, Software, Writing – review & editing

Vladimir Lomonosov: Investigation, Methodology, Resources, Writing – review & editing

Emilie Ringe: Conceptualisation, Funding acquisition, Project administration, Resources, Supervision, Writing – original draft, Writing – review & editing

Conflicts of interest

There are no conflicts of interest to declare.

Acknowledgements

View Article Online
DOI: 10.1039/D6NR00806B

Support for this project was provided by the EU Framework Programme for Research and Innovation Horizon 2020 (ERC Starting Grant SPECs 804523) and the Engineering and Physical Sciences Research Council (EPSCR) grant EP/W015986/1 (MagNanoThermo).

View Article Online
DOI: 10.1039/D6NR00806B

References

(1) Duan, X.; Liu, N. Magnesium for Dynamic Nanoplasmonics. *Accounts of Chemical Research* **2019**, *52* (7), 1979–1989. https://doi.org/10.1021/acs.accounts.9b00157.

(2) Ringe, E. Shapes, Plasmonic Properties, and Reactivity of Magnesium Nanoparticles. *Journal of Physical Chemistry C* **2020**, *124* (29), 15665–15679. https://doi.org/10.1021/acs.jpcc.0c03871.

(3) Appusamy, K.; Blair, S.; Nahata, A.; Guruswamy, S. Low-Loss Magnesium Films for Plasmonics. *Materials Science and Engineering: B* **2014**, *181* (1), 77–85. https://doi.org/10.1016/j.mseb.2013.11.009.

(4) Sterl, F.; Strohfeldt, N.; Walter, R.; Griessen, R.; Tittl, A.; Giessen, H. Magnesium as Novel Material for Active Plasmonics in the Visible Wavelength Range. *Nano Letters* **2015**, *15* (12), 7949–7955. https://doi.org/10.1021/acs.nanolett.5b03029.

(5) Douglas-Gallardo, O. A.; Box, C. L.; Maurer, R. J. Plasmonic Enhancement of Molecular Hydrogen Dissociation on Metallic Magnesium Nanoclusters. *Nanoscale* **2021**, *13* (25), 11058–11068. https://doi.org/10.1039/d1nr02033a.

(6) Gutiérrez, Y.; de la Osa, R. A.; Ortiz, D.; Saiz, J. M.; González, F.; Moreno, F. Plasmonics in the Ultraviolet with Aluminum, Gallium, Magnesium and Rhodium. *Applied Sciences (Switzerland)* **2018**, *8* (1). https://doi.org/10.3390/app8010064.

(7) Farinha, T. G.; Gong, C.; Benson, Z. A.; Leite, M. S. Magnesium for Transient Photonics. *ACS Photonics* **2019**, *6* (2), 272–278. https://doi.org/10.1021/acsphotonics.8b01299.

(8) Honda, M.; Hizumi, K.; Kataoka, A. Nanostructure of Al–Mg System as Novel UV Plasmonic Material. *Optics Communications* **2025**, *591,* 132131. https://doi.org/10.1016/j.optcom.2025.132131.

(9) Hopper, E. R.; Boukouvala, C.; Asselin, J.; Biggins, J. S.; Ringe, E. Opportunities and Challenges for Alternative Nanoplasmonic Metals: Magnesium and Beyond. *Journal of Physical Chemistry C*. **2022**, *126* (26) 10630–10643. https://doi.org/10.1021/acs.jpcc.2c01944.

(10) Vanysek, P. *Handbook of Chemistry and Physics*, 95th ed.; CRC Press, 2015.

(11) Lomonosov, V.; Yang, J.; Fan, Y.; Hofmann, S.; Ringe, E. Stability of Plasmonic Mg-MgO Core-Shell Nanoparticles in Gas-Phase Oxidative Environments. *Nano Letters* **2024**, *24* (23), 7084–7090. https://doi.org/10.1021/acs.nanolett.4c01720.

(12) Pourbaix, M.; Franklin, J. A. *Atlas of Electrochemical Equilibria in Aqueous Solutions*, 2nd ed.; National Association of Corrosion Engineers., 1974.

(13) Niu, K. Y.; Kulinich, S. A.; Yang, J.; Zhu, A. L.; Du, X. W. Galvanic Replacement Reactions of Active-Metal Nanoparticles. *Chemistry - A European Journal* **2012**, *18* (14), 4234–4241. https://doi.org/10.1002/chem.201102544.

(14) Asselin, J.; Boukouvala, C.; Wu, Y.; Hopper, E. R.; Collins, S. M.; Biggins, J. S.; Ringe, E. Decoration of Plasmonic Mg Nanoparticles by Partial Galvanic Replacement. *Journal of Chemical Physics* **2019**, *151*, 244708. https://doi.org/10.1063/1.5131703.

(15) Li, X.; Liu, H.; Yang, J.; Qiao, S. Z.; Du, X. W. Pure Gold Nanocages by Galvanic Replacement Reaction of Magnesium Nanoparticles. *RSC Advances* **2014**, *4* (3), 1185–1188. https://doi.org/10.1039/c3ra45995k.

(16) Lomonosov, V.; Wayman, T. M. R.; Hopper, E. R.; Ivanov, Y. P.; Divitini, G.; Ringe, E. Plasmonic Magnesium Nanoparticles Decorated with Palladium Catalyze Thermal and Light-Driven Hydrogenation of Acetylene. *Nanoscale* **2023**, *15* (16), 7420–7429. https://doi.org/10.1039/d3nr00745f.

(17) Patil, S. J.; Lomonosov, V.; Ringe, E.; Kurouski, D. Tip-Enhanced Raman Imaging of Plasmon-Driven Coupling of 4-Nitrobenzenethiol on Au-Decorated Magnesium Nanostructures. *Journal of Physical Chemistry C* **2023**, *127* (16), 7702–7706. https://doi.org/10.1021/acs.jpcc.3c01345.

(18) Ten, A.; Lomonosov, V.; Boukouvala, C.; Ringe, E. Magnesium Nanoparticles for Surface-Enhanced Raman Scattering and Plasmon-Driven Catalysis. *ACS Nano* **2024**, *18* (28), 18785–18799. https://doi.org/10.1021/acsnano.4c06858.

View Article Online
DOI: 10.1039/D6NR00806B

(19) Smith, J. G.; Yang, Q.; Jain, P. K. Identification of a Critical Intermediate in Galvanic Exchange Reactions by Single-Nanoparticle-Resolved Kinetics. Angewandte Chemie - International Edition. **2014**, *53* (11), 2867–2872. https://doi.org/10.1002/anie.201309307.

(20) Sterl, F.; Linnenbank, H.; Steinle, T.; Mörz, F.; Strohfeldt, N.; Giessen, H. Nanoscale Hydrogenography on Single Magnesium Nanoparticles. *Nano Letters* **2018**, *18* (7), 4293–4302. https://doi.org/10.1021/acs.nanolett.8b01277.

(21) Wayman, T. M. R.; Lomonosov, V.; Ringe, E. Capping Agents Enable Well-Dispersed and Colloidally Stable Metallic Magnesium Nanoparticles. *Journal of Physical Chemistry C* **2024**, *128* (11), 4666–4676. https://doi.org/10.1021/acs.jpcc.4c00366.

(22) Lomonosov, V.; Hopper, E. R.; Ringe, E. Seed-Mediated Synthesis of Monodisperse Plasmonic Magnesium Nanoparticles. *Chemical Communications* **2023**, *59* (37), 5603–5606. https://doi.org/10.1039/D3CC00958K.

(23) Kumar, A.; Villarreal, E.; Zhang, X.; Ringe, E. Micro-Extinction Spectroscopy (MExS): A Versatile Optical Characterization Technique. *Advanced Structural and Chemical Imaging* **2018**, *4* (1), 8. https://doi.org/10.1186/s40679-018-0057-6.

(24) Lowe, D. Distinctive Image Features from Scale-Invariant Keypoints. *International Journal of Computer Vision* **2004**, *60*, 91–110.

(25) Draine, B. T.; Flatau, P. J. Discrete-Dipole Approximation for Scattering Calculations. *Journal of the Optical Society of America A* **1994**, *11* (4), 1491-1499. https://doi.org/10.1364/JOSAA.11.001491.

(26) Boukouvala, C.; Ringe, E. Wulff-Based Approach to Modeling the Plasmonic Response of Single Crystal, Twinned, and Core-Shell Nanoparticles. *Journal of Physical Chemistry C* **2019**, *123* (41), 25501–25508. https://doi.org/10.1021/acs.jpcc.9b07584.

(27) Kopač Lautar, A.; Kopač, D.; Rejec, T.; Bančič, T.; Dominko, R. Morphology Evolution of Magnesium Facets: DFT and KMC Simulations. *Physical Chemistry Chemical Physics* **2019**, *21* (5), 2434–2442. https://doi.org/10.1039/c8cp06171h.

(28) Palik, E. *Handbook of Optical Constants of Solids*; Academic Press, 1998; Vol. 3.

(29) Song, G. L.; Atrens, A. Corrosion Mechanisms of Magnesium Alloys. *Advanced Engineering Materials* **1999**, *1* (1), 11–33. https://doi.org/10.1002/(SICI)1527-2648(199909)1:1<11::AID-ADEM11>3.0.CO;2-N.

(30) Hayden, B. E.; Schweizer, E.; Katz, R.; Bradshaw, A. M. The Early Stages of Oxidation of Magnesium Single Crystal Surfaces. *Surface Science* **1981**, *111*, 26–38.

(31) Nordlien, J. H.; Ono, S.; Masuko, N.; Nisancioglut, K. A TEM Investigation of Naturally Formed Oxide Films on Pure Magnesium. *Corrosion Science* **1997**, *39* (8), 1397–1414.

(32) Yamaguchi, S. Protective Films on Magnesium Observed by Electron Diffraction and Microscopy [4]. *J. Appl. Phys.* **1954**, *25* (11), 1437–1438. https://doi.org/10.1063/1.1721583.

(33) Santamaria, M.; Di Quarto, F.; Zanna, S.; Marcus, P. Initial Surface Film on Magnesium Metal: A Characterization by X-Ray Photoelectron Spectroscopy (XPS) and Photocurrent Spectroscopy (PCS). *Electrochimica Acta* **2007**, *53* (3 SPEC. ISS.), 1314–1324. https://doi.org/10.1016/j.electacta.2007.03.019.

(34) Nordlien, J. H.; Ono, S.; Masuko, N. Morphology and Structure of Oxide Films Formed on Magnesium by Exposure to Air and Water. *Journal of the Electrochemical Society* **1995**.

(35) Rocha, S. D. F.; Mansur, M. B.; Ciminella, V. S. T. Kinetics and Mechanistic Analysis of Caustic Magnesia Hydration. *Journal of Chemical Technology and Biotechnology* **2004**, *79* (8), 816–821. https://doi.org/10.1002/jctb.1038.

(36) Taheri, M.; Phillips, R. C.; Kish, J. R.; Botton, G. A. Analysis of the Surface Film Formed on Mg by Exposure to Water Using a FIB Cross-Section and STEM-EDS. *Corrosion Science* **2012**, *59*, 222–228. https://doi.org/10.1016/j.corsci.2012.03.001.

(37) Liu, M.; Zanna, S.; Ardelean, H.; Frateur, I.; Schmutz, P.; Song, G.; Atrens, A.; Marcus, P. A First Quantitative XPS Study of the Surface Films Formed, by Exposure to Water, on Mg and on the Mg-Al Intermetallics: Al_3Mg_2 and $Mg_{17}Al_{12}$. *Corrosion Science* **2009**, *51* (5), 1115–1127. https://doi.org/10.1016/j.corsci.2009.02.017.

(38) Taheri, M.; Danaie, M.; Kish, J. R. TEM Examination of the Film Formed on Corroding Mg Prior to Breakdown. *Journal of the Electrochemical Society* **2014**, *161* (3), C89–C94. https://doi.org/10.1149/2.017403jes.

(39) Ghali, E. 2 - Activity and Passivity of Magnesium (Mg) and Its Alloys. In *Corrosion of Magnesium Alloys*; Song, G., Ed.; Woodhead Publishing, 2011; pp 66–114. https://doi.org/https://doi.org/10.1533/9780857091413.1.66.

(40) Biggins, J. S.; Yazdi, S.; Ringe, E. Magnesium Nanoparticle Plasmonics. *Nano Letters* **2018**, *18* (6), 3752–3758. https://doi.org/10.1021/acs.nanolett.8b00955.

(41) Hopper, E. R.; Wayman, T. M. R.; Asselin, J.; Pinho, B.; Boukouvala, C.; Torrente-Murciano, L.; Ringe, E. Size Control in the Colloidal Synthesis of Plasmonic Magnesium Nanoparticles. *Journal of Physical Chemistry C* **2022**, *126* (1), 563–577. https://doi.org/10.1021/acs.jpcc.1c07544.

(42) Tcherniak, A.; Ha, J. W.; Dominguez-Medina, S.; Slaughter, L. S.; Link, S. Probing a Century Old Prediction One Plasmonic Particle at a Time. *Nano Letters* **2010**, *10* (4), 1398–1404. https://doi.org/10.1021/nl100199h.

(43) Kelly, K. L.; Coronado, E.; Zhao, L. L.; Schatz, G. C. The Optical Properties of Metal Nanoparticles: The Influence of Size, Shape, and Dielectric Environment. *Journal of Physical Chemistry B* **2003**, *107* (3), 668–677. https://doi.org/10.1021/jp026731y.

(44) Ten, A.; Lomonosov, V.; Boukouvala, C.; Ringe, E. Magnesium Nanoparticles for Surface-Enhanced Raman Scattering and Plasmon-Driven Catalysis. *ACS Nano* **2024**, *18* (28), 18785–18799. https://doi.org/10.1021/acsnano.4c06858.

(45) Xin, Y.; Yu, K.; Zhang, L.; Yang, Y.; Yuan, H.; Li, H.; Wang, L.; Zeng, J. Copper-Based Plasmonic Catalysis: Recent Advances and Future Perspectives. *Advanced Materials* **2021**, *33* (32), 2008145. https://doi.org/https://doi.org/10.1002/adma.202008145.

(46) Swearer, D. F.; Zhao, H.; Zhou, L.; Zhang, C.; Robatjazi, H.; Martirez, J. M. P.; Krauter, C. M.; Yazdi, S.; McClain, M. J.; Ringe, E.; Carter, E. A.; Nordlander, P.; Halas, N. J. Heterometallic Antenna−reactor Complexes for Photocatalysis. Proceedings of the National Academy of Sciences USA **2016**, *113* (32), 8916–8920. https://doi.org/10.1073/pnas.1609769113.

(47) Asselin, J.; Boukouvala, C.; Wu, Y.; Hopper, E. R.; Collins, S. M.; Biggins, J. S.; Ringe, E. Decoration of Plasmonic Mg Nanoparticles by Partial Galvanic Replacement. *Journal of Chemical Physics* **2019**, *151* (24), 244708. https://doi.org/10.1063/1.5131703.

(48) Nayeb-Hashemi, A. A.; Clark, J. B. The Mg-Pt (Magnesium-Platinum) System. *Bulletin of Alloy Phase Diagrams* **1985**, *6* (6), 533–534.

(49) Okamoto, H. Mg-Pd (Magnesium-Palladium). *Journal of Phase Equilibria and Diffusion*. **2010**, 31, 407–408. https://doi.org/10.1007/s11669-010-9732-6.

(50) Nayeb-Hashemi, A. A.; Clark, J. B. *Phase Diagrams of Binary Gold Alloys*; Okamoto, H., Massalski, T. B., Eds.; ASM International, 1987.

(51) Nayeb-Hashemi, A. A.; Clark, J. B. The Cu-Mg (Copper-Magnesium) System. *Bulletin of Alloy Phase Diagrams* **1984**, *5* (1), 36–43.

(52) Naik, A. N.; Patra, S.; Kanekar, A. S.; Sen, D.; Ramagiri, S. V.; Bellare, J. R.; Mazumder, S.; Goswami, A. Nafion Membrane Incorporated with Silver Nanoparticles as Optical Test Strip for Dissolved Hydrogen Peroxide: Preparation, Deployment and the Mechanism of Action. *Sensors Actuators B Chemical* **2018**, *255*, 605–615. https://doi.org/10.1016/j.snb.2017.08.103.

(53) Makar, G. L.; Kruger, J. Corrosion of Magnesium. *International Materials Reviews*. 1993, pp 138–153. https://doi.org/10.1179/imr.1993.38.3.138.

(54) Williams, G.; Ap Llwyd Dafydd, H.; Subramanian, R.; McMurray, H. N. The Influence of Chloride Ion Concentration on Passivity Breakdown in Magnesium. *Corrosion* **2017**, *73* (5), 471–481. https://doi.org/10.5006/2328.

(55) Vermilyea, D. A. The Dissolution of MgO and $Mg(OH)_2$ in Aqueous Solutions. *Journal of the Electrochemical Society* **1969**, *116* (9), 1179. https://doi.org/10.1149/1.2412273.

View Article Online
DOI: 10.1039/D6NR00806B

Data availability

Additional experimental and statistical analysis details and results, Mg nanoparticle size distributions from SEM, UV-Vis-NIR spectra, SEM and HAADF-STEM images, SEM-EDS spectra, single particle optical scattering spectral time series, photographs and spectra taken in the darkfield optical microscope, results of additional numerical calculations, control experiments, and results for the galvanic replacement of Mg nanoparticles by $HAuCl_4$ and Na_2PtCl_4 have been included as part of the Supplementary Information.

The processed data and Python/MATLAB scripts required to produce the figures in the manuscript, as well as Figures S1-S6, S10d, S12, and S14-S16 in the Supplementary Information, are available in Cambridge University's Apollo repository at https://doi.org/10.17863/CAM.127693. Raw hyperspectral data is available upon request.

The code for DDSCAT can be found at http://ddscat.wikidot.com with 10.1364/JOSAA.11.001491. The version of the code employed for this study is version 7.3.2.